From baseline to epileptiform activity: A path to synchronized rhythmicity in large-scale neural networks

Vladimir Shusterman and William C. Troy
Cardiovascular Institute and Department of Mathematics, University of Pittsburgh, Pittsburgh, Pennsylvania 15213, USA
(Received 27 November 2006; revised manuscript received 28 January 2008; published 16 June 2008)

In large-scale neural networks in the brain the emergence of global behavioral patterns, manifested by electroencephalographic activity, is driven by the self-organization of local neuronal groups into synchronously functioning ensembles. However, the laws governing such macrobehavior and its disturbances, in particular epileptic seizures, are poorly understood. Here we use a mean-field population network model to describe a state of baseline physiological activity and the transition from the baseline state to rhythmic epileptiform activity. We describe principles which explain how this rhythmic activity arises in the form of spatially uniform self-sustained synchronous oscillations. In addition, we show how the rate of migration of the leading edge of the synchronous oscillations can be theoretically predicted, and compare the accuracy of this prediction with that measured experimentally using multichannel electrocorticographic recordings obtained from a human subject experiencing epileptic seizures. The comparison shows that the experimentally measured rate of migration of the leading edge of synchronous oscillations is within the theoretically predicted range of values. Computer simulations have been performed to investigate the interactions between different regions of the brain and to show how organization in one spatial region can promote or inhibit organization in another. Our theoretical predictions are also consistent with the results of functional magnetic resonance imaging (fMRI), in particular with observations that lower-frequency electroencephalographic (EEG) rhythms entrain larger areas of the brain than higher-frequency rhythms. These findings advance the understanding of functional behavior of interconnected populations and might have implications for the analysis of diverse classes of networks.

DOI: 10.1103/PhysRevE.77.061911 PACS number(s): 87.18.Sn, 87.19.L−, 87.19.R−

I. INTRODUCTION

Rhythmic activity in the central nervous system ranges from series of action potentials produced by single neurons, to collective oscillations in small neuronal groups, to complex electroencephalographic (EEG) rhythms arising at the level of large neuronal populations [1–3]. A multitude of diverse cellular and network processes drive oscillatory activity at these different levels of organization. On the single neuron level electrophysiological activity (i.e., transmembrane potential) is determined by the flow of ionic currents across the cell's membrane, as described by Hodgkin-Huxley-type formalism. By contrast, activity on the population level arises due to collective synchronization of large pools of neuronal cells [4]. This macroscopic behavior is manifested by field-averaged electrical activity that can be recorded on the scalp or directly on the cortical surface, or tracked indirectly using functional magnetic resonance imaging (fMRI) techniques [1,2,4–8].

The focus of our study is on the theoretical analysis of such macroscopic synchronized rhythmicity. Experimental studies have shown that global synchronization plays a prominent role in normal brain functioning, in particular the dynamics of sleep and wakefulness [9]. Furthermore, synchronized rhythmicity, spreading uncontrollably over large regions of the brain, has been implicated in the pathogenesis of some disorders of the central nervous system, most notably epilepsy [3,10]. Although epilepsy represents a large and heterogeneous group of diseases with different pathophysiological mechanisms, a wealth of evidence from clinical studies strongly suggests that impaired collective functioning of neuronal populations plays a crucial role in a significant proportion of patients with this debilitating disease [1].

Mathematical modeling of the dynamics of large-scale neural networks represents a formidable challenge. In particular, when the Hodgkin-Huxley description of single-cell physiology is applied to model behavior at the global level of the entire brain, both theoretical analysis and numerical simulations quickly become intractable because of unmanageably large numbers of interacting variables [11]. Accordingly, to understand rhythmic behavior at this level, it seems natural to use the coarse-grained (mean) field approach introduced into neuroscience by Wilson and Cowan (WC) [11,12]. This approach, which emphasizes large-scale statistical properties, has proved useful for gaining insight into global dynamical behavior of neuronal populations.

In particular, WC-type models have recently been used to study existence and stability of traveling waves [5,13–15]. Although these studies provided valuable insights into wave dynamics in WC-type neuronal networks, they did not analyze more realistic neurophysiological processes, in particular the formation and evolution of global (EEG) rhythms on the surface of the cortex [2,3]. The analysis of realistic neurophysiological activity in earlier studies has been impeded, at least in part, by the lack of a description of a physiological baseline [16,17]. (As opposed to the mathematical initial rest state, usually represented by zero level of activity, a physiological baseline has nonzero activity [18]). Due to this deficit of knowledge, the pathway from the baseline state to a hyperexcitable state of epileptiform activity has not been studied. Thus, the main objectives of the present study are to examine the following: (i) how a baseline state of electrophysiological activity (see the next section for the definition of baseline) can be reproduced in a WC-type model, and (ii)

how different types of rhythmic behavior, including various synchronized rhythms and epileptiform activity, can arise from the baseline state and spread out spatially due to the interactions of the neural network with various stimuli.

We show how synchronization and loss of synchronization can be predicted by analyzing the interactions between external stimuli, connectivity, and recovery properties of interconnected neuronal populations. We focus on the theoretical understanding of dynamics of epileptiform activity because of its clinical importance, and also because of the experimental data available for validation of our results [3,8].

II. MODEL

We begin by defining a realistic state of baseline physiological activity, which represents activity of the brain in the state of relaxation. In this state, neurons receive some level of spontaneous, weak stimulation by small, naturally present concentrations of neurohormonal substances [19]. The levels of such stimulation vary depending on the relaxation level. In waking adults this state is commonly associated with alpha rhythm, whereas slower rhythms are usually observed during deeper relaxation and sleep [19,20]. These rhythms are almost never stationary, with time-varying frequency and amplitude, as well as other a-periodic patterns [19]. Therefore, the variability of brain activity patterns in such a broadly defined baseline state cannot be described in terms of a single rhythm. As a first step towards modeling a wide range of realistic baseline patterns, we propose the following two-component definition of a baseline state:

(I) A time-independent component represented by subthreshold excitatory activity E and superthreshold inhibitory activity I.

(II) A time-varying component which may include single-pulse waves, multipulse waves, or periodic waves caused by spontaneous neuronal activity [19–21].

This two-component formulation makes the baseline activity definition sufficiently flexible to allow simulation of a variety of rhythmic patterns observed in the cortex, including alpha and slower rhythms, single-pulse and multipulse waves, and the periodic self-production of waves, without periodic forcing or stimuli [6,7,13–15,19,21]. Moreover, this formulation also allows one to reproduce the spontaneous emergence and evolution of different activity patterns due to the system's multistability depending on the initial conditions and inputs, without changes in parameters. Such spontaneous transformations previously were considered impossible in this type of model [22].

Below we show how this baseline state can be reproduced in a WC-type model. We then describe a plausible theoretical path from the baseline state to large-scale self-sustained oscillations, which spread out uniformly from the point of stimulus. For this we modify the recent three-variable extension of the Pinto-Ermentrout WC-type model [13] formulated by Pinto and Troy [23]. The advantage of the latter model in representing a physiological baseline is in its more realistic and balanced representation of the activities of both excitatory and inhibitory neuronal populations [24] compared to the earlier, Pinto-Ermentrout model, which did not include the inhibitory activity and thus represented an unbalanced, excitatory (disinhibited) system [13,25]. Here, we introduce a concept of time-independent activation factors which force the system to undergo a transition from an initial "mathematical" rest state to a state of time-independent baseline activity. The two-dimensional version of the model consists of the following system:

Linear part	Integral part	Time independent activation	Stimulus
$\frac{\partial E}{\partial t} = -E - R$	$+\int_{R^2} \omega_{EE}(x-x',y-y')f(E-\theta_1)dx'dy'$		
	$-\alpha\int_{R^2} \omega_{IE}(x-x',y-y')f(I-\theta_2)dx'dy'$	$+\gamma(x,y)$	$+\Psi(x,y,t),$
$\tau\frac{\partial I}{\partial t} = -I$	$+\int_{R^2} \omega_{EI}(x-x',y-y')f(E-\theta_1)dx'dy'$		
	$-\int_{R^2} \omega_{II}(x-x',y-y')f(I-\theta_2)dx'dy'$	$+\eta(x,y)$	$+\Psi(x,y,t),$
$\frac{\partial R}{\partial t} = \varepsilon(\beta E - R)$			

(1)

TABLE I. Dynamic states of the system and input factors.

State of the system	Input	Dynamics
I. Mathematical rest	$\gamma=0$ and $\eta=0$, $\Psi=0$	$E,I,R=(0,0,0)$
II. Transition from rest to the time-independent baseline: $0<t<T^*$	*Time-independent* activation is introduced: $\gamma>0$ and $\eta>0$; stimulus: $\Psi=0$	System begins its evolution from the rest state (0,0,0) towards baseline; both E and I remain subthreshold: $E<\theta_1$, $I<\theta_2$
III. Time-independent baseline $T^*\leqslant t<T_1$	*Time-independent* activation remains: $\gamma>0$ and $\eta>0$; stimulus: $\Psi=0$	E remains subthreshold but I exceeds threshold uniformly: $E<\theta_1$, $I\geqslant\theta_2$
IV. Time-varying (physiologically relevant) baseline $T_1\leqslant t<T_2$	*Time-independent* activation remains: $\gamma>0$ and $\eta>0$, and in addition, *time-varying* activation (i.e., stimulus) is introduced: $\Psi=\int_{R^2}\omega_{IE}(x',y')dx'dy'+\zeta(x,y,t)$ and the integral term counterbalances effects of inhibitory population.	$E(x,y,t)<\theta_1$, $I(x,y,t)\geqslant\theta_2$ Weak, short-time $\zeta(x,y,t)$ component of stimulus may produce different types of waves [15]
V. Global rhythmic state $t\geqslant T_2$	*Time-independent* activation remains: $\gamma>0$ and $\eta>0$, and *time-varying* activation (stimulus) remains, but the $\zeta(x,y,t)$ component becomes stronger: $\Psi=\alpha\int_{R^2}\omega_{IE}(x',y')dx'dy'+\zeta(x,y,t)$	$E<\theta_1$, $I\geqslant\theta_2$ Strong, short-time $\zeta(x,y,t)$ component of stimulus induces the transition from the baseline state to global rhythmicity, including rotating waves and synchronous oscillations.

In this system a spatial unit (x,y) corresponds to a local neuronal population [12]. The variables $E(x,y,t)$ and $I(x,y,t)$ represent the average activity (i.e., transmembrane potential) levels of the excitatory and inhibitory neuronal populations at the spatial point (x,y) and time t [13,26] with long-range (i.e., nonlocal) connections; R governs the recovery of E [13,14,28,29]. In each equation the integral term with a negative sign in front represents the contribution from the population of inhibitory neurons. Hence, the excitatory and inhibitory connection functions ω_{ij} representing nonlocal influences are always positive and clearly separated. The advantage of such a separation is in its flexibility to model various combinations of the two processes, which might exist in different experimental and clinical settings (at a cost of adding an additional equation to the system). Recently, Kang *et al.* have successfully used the flexibility of this approach to investigate the interactions between the spatial range of inhibition, its time constant, and resulting electrophysiological patterns [27].

Thus, the network (1) is balanced by positive feedback provided by the activity of the excitatory neuronal population E, and negative feedback of the variables I and R. This balance is essential for normal functioning of the system [1–3,18]. The function $f(u)$ defines the sigmoidal-shaped neuronal firing rate; f is approximated by the Heaviside step function [13]; $\omega_{ij}>0$ denotes connectivity from population i to population j and has the typical connectivity form $\omega_{ij}=A_{ij}e^{-k_{ij}\sqrt{x^2+y^2}}$ [in our computations in Eq. (4) we set $\omega_{EE}=2.1e^{-\sqrt{x^2+y^2}}$] [13,14,28,29]. $\alpha>0$ influences the strength of the connections of inhibitory to excitatory neurons; in our study, we assume that $\alpha=1$. Although α could be absorbed into ω_{IE}, we keep it separately for future, more general studies. $\theta_1=0.1$ and $\theta_2=0.1$ are constant threshold levels for E and I [30], τ is the inhibitory time constant (for simplicity $\tau=1$ in our computations) [30], $\varepsilon=0.1$ and β determine the rate of change of R [13,14,28,29]. The time-independent baseline activation factors $\gamma>0$ and $\eta>0$ are introduced as a lumped-parameter representation of intrinsic intracellular and extracellular biochemical processes, including neurohormonal influences, to force the system to evolve from "mathematical" rest to the time-independent baseline. Because our focus is on large-scale functional dynamics (i.e., a large-scale approximation of multiple intracellular and extracellular processes), the detailed characterization of each individual biochemical process lies beyond the scope of this study. The function $\Psi(x,y,t)$ has three components which simulate three different time-dependent physiological stimuli (see Table I),

$$\Psi(x,y,t)=\begin{cases}0, & 0\leqslant t\leqslant T_1,\\ \alpha\displaystyle\int_{R^2}\omega_{IE}(x',y')dx'dy', & T_1\leqslant t\leqslant T_2,\\ \alpha\displaystyle\int_{R^2}\omega_{IE}(x',y')dx'dy'+\zeta(x,y,t), & t\geqslant T_2,\end{cases}\tag{2}$$

where ω_{IE} and $\zeta(x,t)$ are positive, uniformly bounded, and continuous, and $\alpha>0$ is assumed to lie in a bounded range. Note that this form for $\Psi(x,y,t)$ represents a small subset of all possible types of physiological stimuli. It was chosen because it allowed for a plausible simple path to self-sustained rhythmic oscillations, which is the main focus of this study. A number of different stimulus forms have been previously

used to induce a variety of patterns, including solitary and multibump traveling waves, rotating waves [15,25], and spatially uniform self-sustained rhythmic oscillations [8]. Such stimulus-evoked patterns may reflect modifications of neurohormonal concentrations, synaptic transmission, and ionic membrane channel kinetics depending on the type of stimulus and neuronal populations involved [31]. In our model $\Psi(x,y,t)$ is present in both the excitatory and inhibitory parts of Eq. (1), because in most neural architectures the inhibitory neurons receive the same feedforward projections as the excitatory neurons [32,33].

A combination of the activation factor η and stimulus $\Psi(x,y,t)$ in the equation describing the inhibitory activity I is sufficiently general to allow one to obtain a rich variety of dynamical patterns. When η is small and $\Psi(x,y,t)$ is absent (or small), the inhibitory activity I will remain relatively unchanged, leaving the dynamics of the model unchanged as well. On the other hand, when η becomes large enough, it can counterbalance ω_{II} by itself [or in combination with $\Psi(x,y,t)$]. In the Appendix, for mathematical simplicity, we let η itself be large enough to negate the ω_{II} term and to cause I to quickly and uniformly exceed the threshold. The presence of $\Psi(x,y,t)>0$ causes I to exceed the threshold even faster but does not change the dynamics of the system qualitatively. Thus, when η is large, the stimulus $\Psi(x,y,t)$ plays a significant role in the dynamics of the system only in the excitatory part.

Thus, the general structure of Eq. (1) consists of a linear part, an integral part, baseline activation factors, and time-dependent stimuli. The integral part of Eq. (1) represents the effects of activity of all populations through long-range connections. This term is the only source of nonlinearity and nontrivial dynamics in the system. We note that when the activation factors, external stimuli, and connection terms are absent, Eq. (1) reduces to the linear part, and all activity of the network decays to the stable rest state $(E,I,R)=(0,0,0)$. Throughout, we assume that E, I, and R are initially at rest. That is,

$$E(x,y,0)=I(x,y,0)=R(x,y,0)=0 \quad \text{for all } (x,y)\in R^2. \tag{3}$$

We use this initial condition (although this mathematical abstraction is not relevant for a living physiological organism) because Eq. (3) is commonly used in computer modeling as a starting point for simulations. Hence, we also use this condition to provide a common "reference point" for comparison of our investigation with previous modeling studies.

Our goal is to show how the system evolves from the mathematical (nonphysiological) rest state (3) to a realistic state of baseline physiological activity, as defined at the beginning of this section. As explained above, this process consists of two stages (Table I). First, the system evolves into the time-independent baseline state (Table I, part II), where E and I have reached constant levels of activity which are uniformly close to their respective time-average levels. Because electrophysiological rhythms (α or θ) in this relaxed state are relatively slow, the time-average level of such activity (i.e., excitatory activity E) would be below its threshold ($E<\theta_1$). Since the excitatory and inhibitory activities are usually reciprocal [24,34], one can assume that this effect is due to the suprathreshold level of the inhibitory activity I ($I\geqslant\theta_2$),

$$E(x,y,t)<\theta_1 \quad \text{and } I(x,y,t)\geqslant\theta_2 \text{ for all } (x,y)\in R^2.$$

This non-zero-activity state is more realistic for a living organism than the initial zero-activity mathematical rest state. However, the system does not yet exhibit realistic, time-varying, rhythmical behavior. For this reason, we have added the second time-varying component of baseline. A description of the dynamic process that leads to the baseline state through the activation factors γ and η, and appropriately timed stimuli Ψ is given in Sec. II A. Further mathematical details are provided in the Appendix. We also describe two additional mathematical properties which are needed for the transition from the baseline state to a state of epileptiform activity (Sec. II B and Sec. II C). These include oscillatory properties of the linear part of the model (Sec. II B), and global bistability properties (Sec. II C). Finally, we show how a dynamical process, combining the properties described by all three principles, can form a physiologically plausible path to synchronized rhythmic activity in Eq. (1). In numerical experiments we demonstrate how synchronous self-sustained oscillations (SSO) arise, spread, and interact, and how these dynamics are consistent with neurophysiological experiments [5,8].

We now describe three mathematical properties, summarized for clarity in the form of principles, which give sufficient conditions for spontaneous self-organization in Eq. (1).

A. Principle I

The network can be transformed into a reduced, positive feedback system. A combination of the time-independent activation factors and time-dependant stimuli is required to counterbalance the negative feedback of variables R and I and transform (1) into a positive-feedback system capable of self-organization. Recall from Eq. (3) that the solution of Eq. (1) is initially in the stable ("mathematical") rest state $(E,R,I)=(0,0,0)$. The transformation begins when we let the baseline activation factor η be of sufficient magnitude to cause the tonic activity of the inhibitory neurons (I) to quickly and uniformly increase to its threshold level θ_2. When this threshold is reached at a critical time $t=T^*$ the system has undergone the transition from rest to the time-independent baseline, and the first step of the transformation is complete (Table I, parts I–II) [17]. Details of this transition are given in the Appendix. Over the interval $[0, T_1]$ the variables E and R remain practically unchanged because their response time to the activation factors is relatively slow compared to that of I (see the Appendix). For $t\geqslant T^*$ the system remains in this state until $t=T_1>T^*$ when a stimulus Ψ is applied which causes the (E,I,R) network Eq. (1) to transform into a time-varying baseline state in which the activity of the inhibitory population I is temporarily counterbalanced (Table I, part III). As Table I (part III) shows, the integral part of Ψ determines the minimal magnitude of the stimulus required to counterbalance (block) the effects of the inhibitory neuronal population [when $\zeta(x,y,t)=0$]. The magnitude

of Ψ remains relatively small as long as its $\zeta(x,y,t)$ component is weak. Such weak stimuli can produce different types of waves depending on γ, but no self-sustained oscillations. For $t>T_1$ the system remains in this time-varying baseline state until a sufficiently strong stimulus $\zeta(x,y,t)$ is applied at a time $t=T_2$, and subsequently the system dynamics evolve into rhythmic synchronized oscillations (Table I, parts IV). In the Appendix we also show how a rescaling transforms the time-varying baseline (E,R) system into the positive-feedback system

Linear part	Integral part	Stimulus

$$\frac{\partial u}{\partial t} = -u - v + \int_{R^2} \omega_{EE}(x-x',y-y') \times f(u-\theta)dx'dy + \zeta(x,y,t)$$

$$\frac{\partial v}{\partial t} = \varepsilon(\beta u - v) \tag{4}$$

Here ω_{EE} is positive, continuous, integrable, symmetric, and has the typical connectivity form described in the model section earlier [13,14,28,29]. The parameters $\varepsilon>0$ and $\theta>0$ are constants; $\beta(x,y)=\gamma(x,y)/\text{const}-1$ represents local recovery properties modulated by the baseline activation factor γ (see the Appendix). The function β plays a particularly important role in the development of different patterns of electrophysiological activity, including traveling activity waves and the self-assembly of neuronal populations into synchronously oscillating functional groups [2]. This is consistent with observations that the time course of the relative refractory rate of the neurons plays an important role in the dynamics of neuronal bulks [3]. Because E and R do not change significantly from the rest level $E=R=0$ over the time interval $0 \leqslant t \leqslant T_2$, we assume that

$$u(x,y,T_2) = v(x,y,T_2) = 0 \quad \text{for all } (x,y) \in R^2. \tag{5}$$

Below, in Secs. II B and II C we describe two additional properties of Eq. (4) which are needed for the transition from the time-independent baseline to the time-varying baseline state.

B. Principle II

The linear part of the positive-feedback network (4) exhibits decaying oscillations whose frequency increases without bound as β increases. To understand how oscillations arise in the linear part of Eq. (4) we study

$$\frac{\partial u}{\partial t} = -u - v,$$

$$\frac{\partial v}{\partial t} = \varepsilon(\beta u - v). \tag{6}$$

We let β be a constant and examine the effects of the associated eigenvalues $\lambda^{\pm}=[-(\varepsilon+1)\pm\sqrt{(\varepsilon-1)^2-4\varepsilon\beta}]/2$ over different ranges of β. When β is small, $\lambda^{\pm}$ are real and negative, and solutions of Eq. (6) cannot oscillate. Instead, they monotonically approach the constant state (0,0) in the (u,v) phase plane. When $\lambda^{\pm}$ are real, the only patterns of functional activity in Eq. (4) that can be initiated by the stimulus ζ are solitary traveling waves or wave fronts [15]. When β increases and passes the critical value $\beta_*=(1-\varepsilon)^2/4\varepsilon$, the eigenvalues become complex; all nontrivial solutions of Eq. (6) are now oscillatory and spiral into the constant state (0,0) in the (u,v) phase plane. The frequency of these oscillations is given by $\sqrt{4\varepsilon\beta-(\varepsilon-1)^2}/4\pi$; as β increases from β_*, the frequency rises without limit.

C. Principle III

At a critical $\beta^*>\beta_*$ bistability occurs in the positive-feedback network: a stable, spatially independent, periodic solution and a stable rest state coexist over a continuous range of parameters. To understand how bistability occurs in Eq. (4), we study spatially independent solutions. These solutions satisfy

$$\frac{\partial u}{\partial t} = -u - v + f(u-\theta),$$

$$\frac{dv}{dt} = \varepsilon(\beta u - v). \tag{7}$$

When $0<\varepsilon<1$ and the activation threshold θ is relatively small (e.g., $\varepsilon=0.1$ and $\theta=0.1$), there is a second critical value $\beta^*>\beta_*$ such that if $\beta \geqslant \beta^*$ then Eq. (7) has a stable periodic solution (whereas no periodic solutions exist when $\beta<\beta^*$). An example of such periodic solutions is shown in the second row of Fig. 1.

Figure 1 also illustrates how system Eq. (7) exhibits increasingly oscillatory patterns of solutions as β increases from β_*. These patterns include monotonic damping (top row), damped oscillations (second row), and the transition to bistability in which stable periodic solutions coexist with one or more stable rest states (third and fourth row). A standard phase-plane topological shooting argument can be used to prove the existence of the periodic solutions in Fig. 1.

D. Emergence of SSO

We now show how these principles lead to the initiation and spread of self-sustained synchronous oscillations (SSO) in the positive-feedback system (4); for simplicity, this process is analyzed in one dimension (Fig. 2). Numerical simulations confirm that the same process holds in two dimensions [Fig. 3(a)]. Because all three principles are invariant with respect to dimension, we conjecture that our results also hold in three dimensions. It is possible to couple two separate three-dimensional systems of the form (E,I,R) together to model interaction across cortical layers.

The first step of the process is described by Principle I (see the appendix for details) which shows analytically how appropriate activation factors quickly transform the dynam-

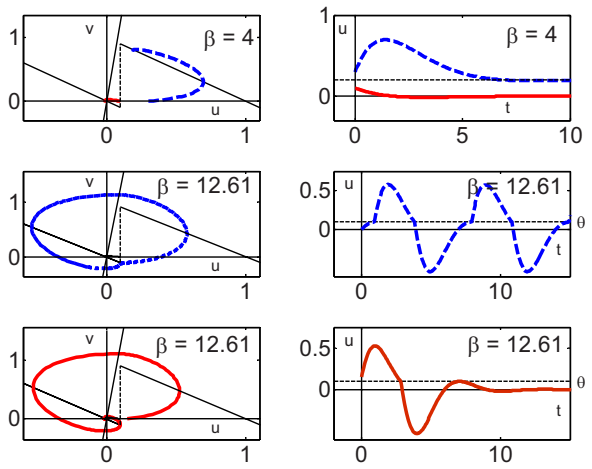

FIG. 1. (Color online) Phase portraits (left) and corresponding time plots (right) of spatially independent solutions of Eq. (7) when $(\varepsilon,\theta)=(0.1,0.1)$. Top row: When $\beta=4<\beta^*=12.61$, all solutions monotonically approach a constant state. Second row: When $\beta=\beta^*$, a stable periodic solution emerges if the stimulus $\zeta(x,y,t)$ is sufficiently strong. Third row: In addition to the stable periodic solution shown in the second row, the system has the stable rest state at (0,0), which attracts solutions initiated by lower-amplitude stimuli. Therefore, the system is bistable. See Table I for details.

ics of Eq. (1) into those of the canonical positive-feedback network (4).

The next step is to understand the dynamics of Eq. (4) when the recovery function β is held constant at a level $\beta \geqslant \beta^*$. To initiate an SSO, a stimulus is applied at an arbitrarily chosen spatial point [Fig. 3(a)]. By Principle III, there is a stable, spatially independent, periodic solution (i.e., a bulk oscillation), which causes the solution of Eq. (4) to begin oscillating at the point of stimulus. Subsequently, at nearby points, the solution also begins to oscillate; these oscillations become spatially uniform and in phase over a gradually expanding region, referred to as the SSO region, or equivalently, the region of synchrony (Fig. 2, rows 2 and 3) (supplementary movie S1 [52]).

The rate of expansion of the SSO region is determined by an interplay between two key features: (i) the speed c of waves that form and propagate outward from the edge of the region, and (ii) the concave shape of the graph of the activation variable u as it rises, during each cycle, from the resting state $u=0$ to the activation threshold level θ (Fig. 4). [The exact point where the concave region starts is given by $\frac{u_t}{u}=-\frac{\varepsilon(\beta+1)}{1+\varepsilon}$; u is negative at this point. However, the maximal concavity of the solution occurs over the time interval on which u increases from 0 to θ. During this subthreshold interval, whose length is denoted by Δt, the solution satisfies Eq. (6), which is equivalent to $u_{tt}=-(1+\varepsilon)u_t-\varepsilon(\beta+1)u$.] Thus, u_{tt} is negative and u is concave since u_t and u are both positive as u rises from $u=0$ to $u=\theta$. Due to concavity, it takes a relatively long time (Δt) for the activation u to reach its threshold θ.

From our numerical experiments we observed that during the rise of a solution towards threshold, as the rate of vertical increase slows down due to the concave component, the

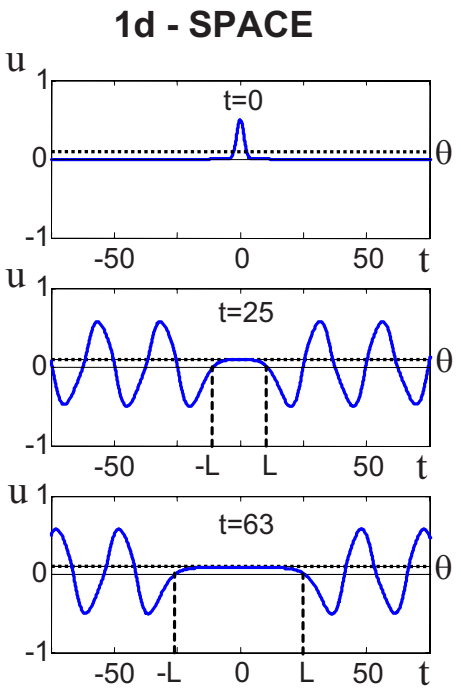

FIG. 2. (Color online) From top to bottom: Progressive growth of the region of self-sustained synchronous network oscillations in one dimension; $\beta=12.61$, $\omega(x)=0.5e^{-|x|}$. See supplementary movies S1 and S2 see [52]. Synchronous oscillations emerge following *a* stimulus (top) and gradually expand outwards, as the entire network synchronizes (second and third panels).

stable solitary wave emanating from the region of SSO causes the region to expand spatially at a rate proportional to the wave speed. From this initial observation it was natural to expect that the proportionality constant should be the fraction of the time that the solution is concave during one cycle. This led us to conjecture formula (8) below, which predicts the rate of migration of the leading edge of the SSO region (*rate*), and its validity was borne out by numerical experiment (Table II). The *rate* (R) is determined by a product of two factors, the fraction $\Delta t/T$, where T is period of each oscillation, and the wave speed c,

$$R=\frac{\Delta t}{T}c. \tag{8}$$

Our numerical simulations show that the *rate* calculated using formula (8) gives a $<1\%$ error per cycle of SSO (or equivalently, $<15\%$ cumulative error until the leading edge of the region of SSO reaches $x=100$) of the numerically computed solutions. Since $0<\Delta t/T<1$, Eq. (8) shows that the migration rate of SSO is a fraction of the speed of traveling waves, which is consistent with experimental and clinical observations regarding the spread of epileptic activity [3]. In addition, simulations show that the ratio $\Delta t/T$ and the speed c both decrease as β increases (Table II). The mechanism described above provides a plausible explanation for sustenance of epileptiform activity without a hypothetical driving source that, despite a number of experimental studies, has never been observed [3].

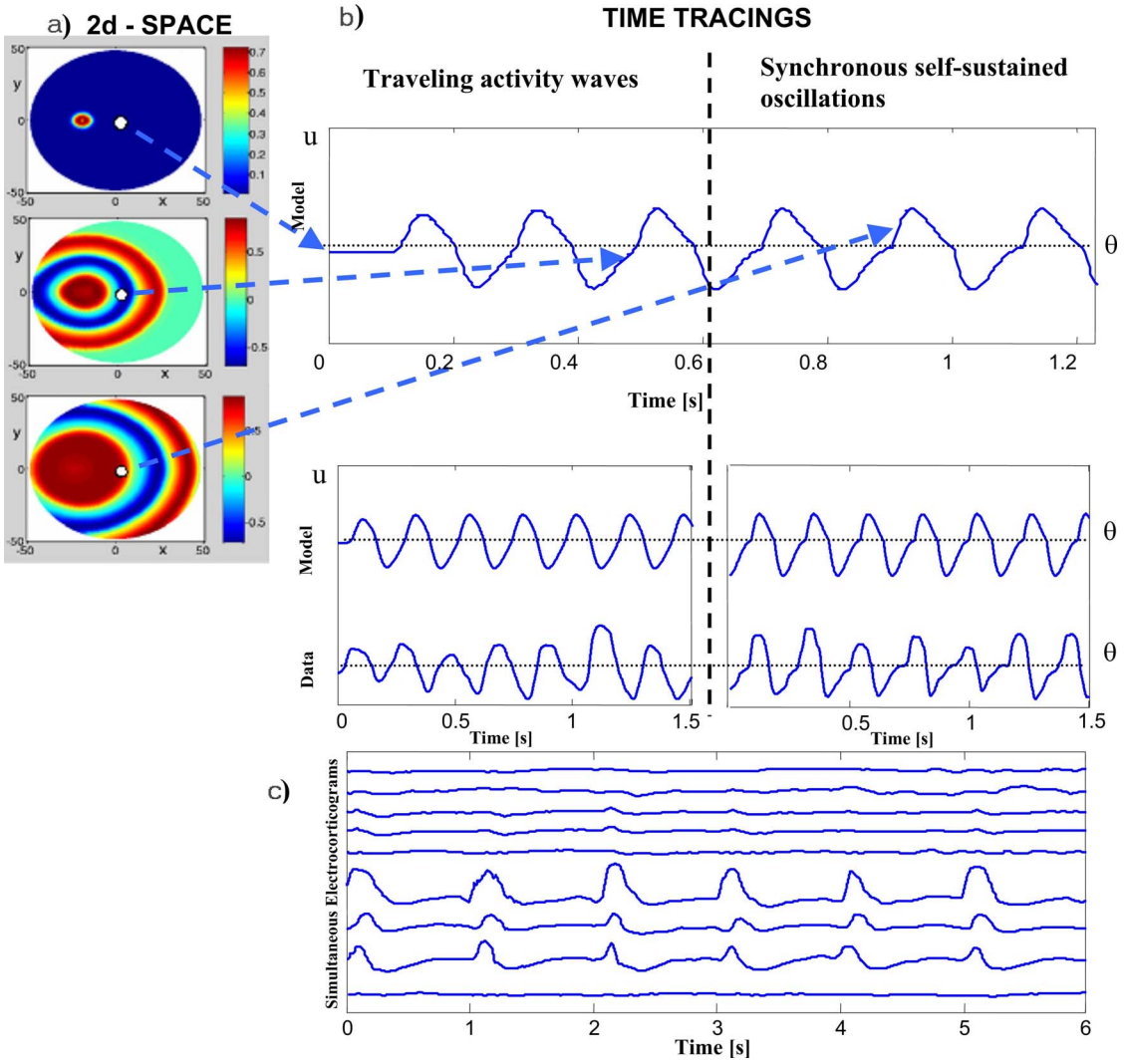

FIG. 3. (Color online) (a) from top to bottom: Progressive growth of the region of self-sustained synchronous network oscillations in two dimensions (see supplementary movies S1 and S2 [52]). Synchronous oscillations that emerge following a stimulus (top) gradually expand outwards, as the entire network synchronizes (bottom). (b) Top: Time series of electrical activity registered by a single electrode shown by a white dot in (a). The first three traveling activity waves are followed by three SSO oscillations. Horizontal dotted line indicates activation threshold. The initial subthreshold segment of the traveling wave is convex, whereas that of the SSO is concave. The transition from traveling waves to SSO occurs between the third and fourth cycle. Bottom: Comparison of traveling activity waves (left) and SSO (right) in the model with corticographic data recorded from one of the electrodes located on the surface of the brain during migration of seizure activity across the region of the recording electrodes. The bottom row shows the dynamics of electrical activity recorded directly from an electrode chronically implanted onto the surface of the brain (right parietotemporal area) during migration of seizure activity across the recording region in a 7-year old female [8]. (c) Direct (subdural) electrocorticographic recordings obtained during seizures from chronically implanted electrodes (10 mm center-to-center spacing) on the surface of the left temporal lobe of a 52-year old female [8]. Note that large-amplitude oscillatory pattern of activity at three neighboring electrodes has identical frequency and phase; the activity is relatively quiescent at the rest of the recording sites. Note also that a slowly rising region precedes each large spike. These properties strongly suggest that an entire region has become synchronized, in agreement with predictions of the model.

E. Comparison of the theoretically predicted and experimental *rate* in a human case study

To compare the *rate* predicted by formula (8) with experimental data obtained by Towle *et al.* [8] by placing an array of recording electrodes on the cortical surface of a human subject experiencing epileptic seizures, we estimated the period T and the length Δt of the concave segment in each oscillatory wave form of the human corticographic recording in Fig. 3(b) (bottom-right tracing marked "data," under the heading "synchronous self-sustained oscillations"). Using this estimation, we found that the values of T and Δt in each cycle lie in the ranges

$$0.21\ \text{s} \leqslant T \leqslant 0.22\ \text{s} \quad \text{and} \quad 0.03\ \text{s} \leqslant \Delta t \leqslant 0.05\ \text{s}.$$

From these estimates we obtained the range $0.136 \leqslant \frac{\Delta t}{T} \leqslant 0.238$. Substituting these bounds into formula (8), and using experimentally measured wave speed c in the human

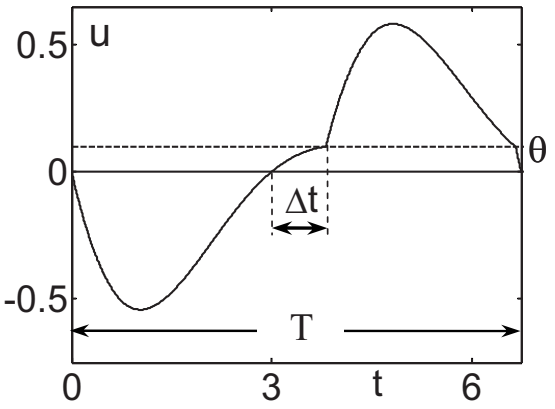

FIG. 4. The graph of the activity variable **u** during a single cycle of SSO oscillation for $\beta=12.61$. When u rises from the resting state 0 to the threshold θ, the shape of the graph is concave. The concavity of u on this interval, of length Δt, is one of the key features determining the rate of expansion of the region of SSO.

visual cortex (22.4 mm/s [35]), we obtain the range of *theoretically predicted rate* (R_T),

$$3.046 \text{ mm/s} \leqslant R_T \leqslant 5.331 \text{ mm/s}. \tag{9}$$

Next, we estimated the rate of migration of the leading edge of synchronized oscillatory activity from the simultaneous multielectrode "maps" of cortical activity constructed by Towle *et al.* [8], which gave an *experimentally measured* $R \approx 4$ mm/s. Note that the experimentally measured R is within the range of the theoretically predicted values given in Eq. (9), despite the approximate values used in these computations. Summarizing, the ratio R/c predicts that the leading edge of the region of synchronous seizure activity migrates approximately 4–7 times slower than normal brain wave activity, which is not in disagreement with the results of human case study of epileptic seizures reported by Towle *et al.* [8] These preliminary data also suggest that further research into the accuracy and generalizability of formula (8) for different populations and types of epileptiform activity is warranted. In particular, longer recordings from densely spaced electrodes will provide more accurate measurement of the values of T and Δt and their spatial and temporal distributions, allowing more rigorous validation of formula (8).

Peskin, and Mirollo and Strogatz describe similar concavity-delay mechanisms in their analyses of synchronized behavior of cardiac cells and populations of fireflies [36,37]. They found that concavity is a necessary condition for synchronization to occur. In particular, they used the concave component of the curve between the baseline rest state and threshold in the analysis. Here, we have extended their results by introducing a formula that estimates the rate of expansion of the synchronizing region with the use of both the positive part of the concavity and the speed of a stable solitary wave (supplementary movie S3 [52]).

The models used by Peskin, and Mirollo and Strogatz represent arrays of coupled oscillators, each one describing the repetitive firing of an individual cardiac cell or a firefly. Our model is different because no self-sustained oscillations emerge without an appropriate stimulus. Indeed, if a stimulus at a given point is not sufficiently strong, the SSO phenomenon does not occur. Instead, the solution evolves into a pulse-shaped traveling wave (supplementary movie S3 [52]). However, when an initial stimulus is of sufficient magnitude, oscillations do emerge and spread outwards from the point of stimulus.

The first row of Fig. 3(b) shows the time tracing of a solution of Eq. (4) at a single recording site (white dot in Fig. 3(a)). Initially, the recording site is outside of the SSO region. In the time tracing the shape of the subthreshold section during the first three oscillations is convex, indicating that these oscillations represent traveling waves of activity because the recording site is outside the region of synchrony. However, during the 4–6th oscillations the shape of the subthreshold activity has changed from convex to concave, which shows that the leading edge of the SSO region has reached the recording site. This change from convex to concave shape is in agreement with the theoretical predictions that follow from our analysis. Recent neurophysiologic studies in rat hippocampus have confirmed, both in vitro and in vivo, the existence of the subthreshold slowly rising, concave-form activation that precedes the action potential upstroke [38]. Experimental evidence suggests that this phenomenon represents activation of a subpopulation of neurons that escape inhibitory influences due to heterogeneous connections or irregular spread of activity [38].

The dynamic behavior described above has also been observed by Towle *et al.* [8] in human studies of electrical activity in the brain. The second row of Fig. 3(b) compares the dynamics of electrophysiological activity at a single site

TABLE II. The rate of spread of the region of SSO for different values of β. R_T is the rate predicted using formula (8); R_C is the rate calculated in computer experiments using the time required for the leading edge of the region of SSO to reach $x=100$; $E_{x=100}$, the error between R_T and R_C representing the error accumulated over all oscillatory cycles required for the leading edge of the region of SSO to reach $x=100$; N_c, the number of oscillatory cycles required for the region of SSO to reach $x=100$; $E_c=(1/N_c)E_{x=100}$.

β	Δt	T	$\Delta t/T$	c	R_T	R_C	$E_{x=100}$	N_c	E_c
12.61	0.780	7.248	0.108	3.665	0.394	0.442	0.122	31.181	3.91×10^{-3}
14	0.585	6.225	0.093	3.624	0.338	0.370	0.0947	43.373	2.18×10^{-3}
15	0.510	5.910	0.086	3.593	0.310	0.325	0.0484	52.115	9.29×10^{-4}
16	0.465	5.655	0.082	3.563	0.293	0.331	0.130	53.404	2.43×10^{-3}
17	0.420	5.415	0.077	3.532	0.272	0.306	0.125	60.388	2.07×10^{-3}

in the model with activity registered by an electrode chronically implanted directly onto the surface of the human brain [8]. This human subject undergoes an electrocorticographic recording during migration of seizure activity across the region of recording electrodes. These experiments capture the dynamics of the onset and spread of SSO. In particular, the second row of Fig. 3(b) shows how a pattern of electrical activity changes from traveling waves when the seizure activity is outside of the recording electrode, into large-amplitude, self-sustained oscillations (SSO) when the seizure activity is directly under the electrode. Note the remarkable similarity between the patterns of model-generated (row 1) and neurophysiologic data (row 2) showing traveling waves and bulk oscillations (SSO). During each upstroke concavity is clearly visible in the sub-threshold interval of the SSO patterns but not in the traveling waves. Figure 3(c) shows electrophysiologic data obtained from an array of electrodes chronically implanted on the surface of the brain in another human subject also suffering from intractable epilepsy [8]. Note that three electrodes record synchronous large-amplitude oscillations, whereas activity is relatively quiescent at the rest of the recording sites. The uniformity of frequency and phase strongly suggests that the large-amplitude synchronous oscillatory activity represents persistent bulk oscillations in an entire spatial region containing the three recording electrodes. It is interesting to compare the frequency of oscillations in Figs. 3(b) (second row) and 3(c). The large-amplitude synchronous oscillations entraining the entire region sampled by the three recording electrodes [Fig. 3(c)] are several times slower than those migrating across the region of recording electrodes [second row of Fig. 3(b)] [8]. Again, the observation that persistent, spatially uniform oscillations over a relatively large region are associated with the slower rhythm [Fig. 3(c)] agrees with the theoretical predictions of Eq. (8).

F. A kindling-type interaction

A kindling-type interaction, in which epileptiform activity spreads from one region to another has been well documented [39]. To investigate the rules of interaction between neighboring regions, we consider distinct spatial regions with different synchronization properties

The first row of Fig. 5 shows distinct disk-shaped regions D_1 and D_2, which are separated by a "buffer" region, and with two different β values, β_1 and β_2, such that $\beta^* \leqslant \beta_1 < \beta_2$. This allows synchronization to occur in both regions.

However, $\beta < \beta^*$ outside and between these regions, so that synchronization does not occur in the buffer region. Since β_1 and β_2 are completely independent of each other, the difference between the two β values can be large and the two regions can synchronize at substantially different rates. An initial stimulus is given at the center of D_1 (left). As the solution synchronizes in D_1, activity waves propagate outwards and trigger synchronization in D_2. Subsequently, the SSO region D_2 also starts emitting activity waves. Because the region between D_1 and D_2 is relatively large, the activity waves coming from D_1 meet and annihilate the waves coming from D_2. In the buffer region, synchronization is not possible since $\beta < \beta^*$. The end result is that the regions D_1 and D_2 remain synchronized at two distinct frequencies (supplementary movie S4 [52]). Because $\beta_1 < \beta_2$, the uniform oscillations in D_1 have lower frequency than in D_2 However, as formula (8) shows, the rate of synchronization in D_1 is faster than in D_2. These results give a plausible explanation of how remote sites can synchronize in the brain and, as noted above, are consistent with observations that lower-frequency EEG rhythms entrain larger areas of the brain than higher-frequency rhythms [2]. Our finding that synchronization spreads most efficiently at slower frequencies is also consistent with recent fMRI data, corresponding to local-field neural activity [4], which show a stronger spatial response to lower-frequency visual stimuli [40].

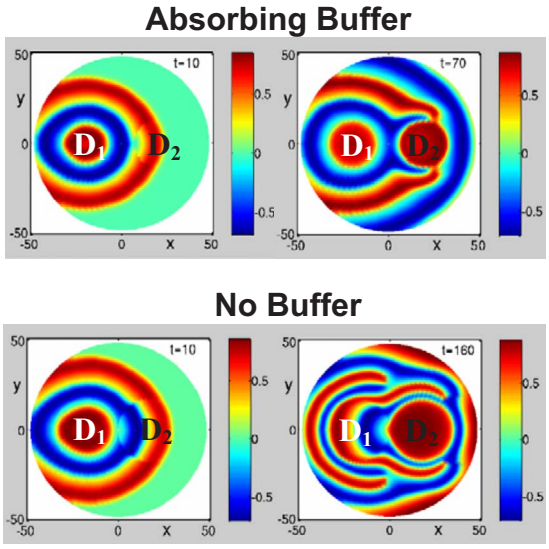

FIG. 5. (Color online) Interaction between low-frequency and high-frequency SSO in distinct regions. Top row: $\beta_1 = 12.61 = \beta^*$ inside the disk-shaped region $D_1: (x+20)^2 + y^2 \leqslant 100$; $\beta_2 = 15$ inside the region $D_2: (x-20)^2 + y^2 \leqslant 100$; $\beta = 7$ otherwise. Bottom row: β_1, β_2 have the same values as above, but now D_1 and D_2 are close to each other: $D_1: (x+20)^2 + y^2 \leqslant 400$, $D_2: (x-20)^2 + y^2 \leqslant 400$. See text for details.

In the second row of Fig. 4, the two disk-shaped regions have the same β values as above, but now D_1 and D_2 are close to each other and the size of the buffer region is significantly reduced. Again, an initial stimulus given at the center of D_1 causes synchronization to begin; in turn, activity waves are formed and emitted outwards. These waves trigger synchronization in D_2, and activity waves are also emitted from region D_2. However, because the buffer region is small, the activity waves from D_2 enter D_1 and quickly annihilate synchronization in D_1. The end result is that synchronization persists only in region D_2 (supplementary movie S5 [52]). Thus, we conclude that when the buffer is small, the region with higher-frequency oscillations dominates and inhibits synchronization in the slower-oscillating adjacent region.

Our experiments indicate that two complete wavelengths of the traveling wave is the minimal buffer width. When the disks are located closer, the wave emanating from the faster oscillating region enters the other region before the slower oscillating region can emit a wave. Because these waves

have to meet in the buffer region to annihilate each other, a smaller buffer region would not allow this annihilation phenomenon to occur. Thus, if the buffer region is smaller than two complete wavelengths of the traveling wave, waves from the faster oscillating region (higher β) will successfully reach the other region and interfere with the synchronization in that region. We found in our experiments that even a unit-size disk emits traveling waves as synchronization develops and can trigger synchronization in other regions that are located at least two wavelengths away.

III. CONCLUSIONS

Our study has shown how a neural network can undergo a series of transformations from the "mathematical" rest to physiological baseline and ultimately, rhythmic, self-sustained epileptiform activity.

We have also shown that the emergence of synchronous self-sustained oscillations in large-scale population networks can be anticipated when the following three principles hold: (1) The network with both positive and negative control mechanisms can be transformed into a strictly positive-feedback system by activation factors and external stimuli, (2) the linear part of the positive-feedback system exhibits decaying oscillations whose frequency increases without bound as β increases, and (3) at a critical β^*, stable, spatially independent, periodic solution comes into existence and coexists with a stable rest state over a continuous range of parameters. These principles depict sufficient conditions for the spontaneous development of synchronous oscillations in complex, multicomponent networks. Furthermore, our study explicitly links the emergence and spread of self-sustained synchronized oscillatory activity with the modification of recovery properties of the network by stimuli. As β varies from 0 to β^*, our model is capable of reproducing a number of dynamic phenomena, including wave fronts, solitary, and multibump waves, as well as the self-sustained periodic formation of traveling waves, and also rotating waves. All of these phenomena have been observed in neurophysiological experiments [5,10,25,41]. We address mathematical properties of these types of solutions elsewhere [15].

Our work further extends a large body of work on pattern formation, including global oscillations (i.e., cortical synchronization) and more complicated behavior, that have been well documented in neural field models [26,42]. Similar field models with nonlocal coupling have been described by Ermentrout [26], Gerstner and Kistler [43], Coombes [44], and Bojak and Liley [42]. Our work further extends these studies and provides results with respect to the refractory variable R as well as the specific forcing [the activation factors γ and η, and stimulus function $\Psi(x,y,t)$] that effectively force the system to undergo a series of transformations from mathematical rest to the baseline state and, ultimately, to self-sustained oscillatory activity. In contrast to previous studies, we have found that the self-organization process does not depend on the presence of noise or *a priori* built-in periodic forcing [45,46]. Instead, this is a result of the intrinsic dynamics of population networks characterized by strong, long-range connectivity.

Previously, Bojak and Liley have reproduced a realistic spectrum of electrophysiological activity in a mean-field model [21]. In this study, we did not attempt to reproduce a realistic power spectrum which represents a combination of a number of electrophysiological processes. Theoretically, it is possible to extend our approach in this direction by adding more appropriately chosen components to the stimulus function $\Psi(x,y,t)$. However, our goal was to describe general properties (principles) of the system dynamics and transformations from mathematical rest to a more realistic (time-varying) state, here referred to as the time-varying baseline, and finally to a state of SSO.

Our analysis uncovers a plausible transition from baseline activity patterns to synchronized epileptiform rhythmicity. More elaborate versions of WC-type models, including those of the thalamocortical networks with multiple modules and subunits [47] or detailed synaptic interactions [21,48], have also been used to reproduce epileptiform activity. By contrast, our model is substantially simpler, hence it is more general and theoretically tractable at the expense of a less detailed description of brain architecture and synaptic interactions.

Our findings that rhythmicity can arise in complex, multicomponent networks as a result of dynamic, self-organizing behavior without periodic driving force may be relevant to the analysis of slow rhythms in the cardiac, respiratory, and vascular neurohormonal regulation which remain largely unexplained [49–51]. Of particular interest for future studies is to determine the types of epileptiform activity and patient populations for which formula (8) can predict the rate of migration of the leading edge of synchronous oscillations. It also important to determine whether our three principles are not only sufficient, but necessary for spontaneous self-organization. Thus, analysis of theoretical principles and functional behavior of neural networks presented here might be useful for gaining insights into the origins and spread of epileptiform activity and other important problems of contemporary neuroscience.

ACKNOWLEDGMENTS

The authors would like to thank Dr. G. Buzsaki for helpful comments and suggestions. The research of V.S. was supported in part by Grant No. R44HL077116 from the National Heart, Lung, And Blood Institute. The research of W.C.T. was supported by NSF Grant No. DMS0412370.

APPENDIX

In this section we show how system (1) which is initially in State I (Table I), mathematically characterized by

$$E(x,0) = I(x,0) = R(x,0) = 0 \quad \text{for all } x, \tag{A1}$$

undergoes a transition to State III (Table I) which is mathematically expressed as

$$E(x,t) < \theta_1 \quad \text{and } I(x,t) \geqslant \theta_2 \quad \text{for all } x. \tag{A2}$$

For simplicity, we carry out the analysis in one dimension. However, all details are exactly the same in two and three

dimensions. We follow a two-step process. First, we make simple, general assumptions on the baseline activation factors γ and η, and stimulus Ψ, and determine global bounds on functions and parameters which appear in the model. Second, we make use of these assumptions and bounds and carry out the analysis.

1. Assumptions and global bounds

First, we assume that the activation factor $\eta(x)$ is stronger than $\gamma(x)$. Our analysis will show how this assumption contributes to achieving and maintaining subthreshold level of activity of the excitatory population in the time-independent baseline state (Table I, part III). Specifically, we assume the following:

(i) Let $L>0$ and $\theta_3 \in (\frac{\theta_1}{2}, \theta_1)$ be fixed. Assume that $\gamma(x)$ is continuous and satisfies

$$0 < \theta_1 - \theta_3 \leqslant \gamma(x) \leqslant L(\theta_1 - \theta_3) \quad \text{for all } x, \tag{A3}$$

where $\theta_1 - \theta_3 > 0$ and sufficiently small so that $\gamma(x)$ is uniformly small.

(ii) For simplicity, we assume that $\eta(x)$ is constant and has the form

$$\eta = \int_R \omega_{II}(x')dx' + (1+\delta)\theta_2. \tag{A4}$$

We also assume that the activation factor $\eta(x)$ is uniformly large for all $t \geqslant 0$. This is achieved by letting $\delta > 0$ be large. As we shall show, this causes the activity level of the inhibitory neurons to rapidly increase until a time T^* is reached where I uniformly exceeds its threshold θ_2. In particular, we will show that the inhibitory activity I remains above θ_2 when $t \geqslant T^*$. That is,

$$I(x,t) \geqslant \theta_2 \quad \text{for all } t \geqslant T^* \text{ and } x. \tag{A5}$$

Physiologically, inequality (A5) corresponds to the state of tonically active inhibition [18,22].

Definition of β. We define

$$\beta(x) = \frac{\gamma(x)}{\theta_1 - \theta_3} - 1 \quad \text{for all } x. \tag{A6}$$

We will investigate system dynamics for both constant and spatially variable β.

Global bounds. We now obtain global bounds which are needed in the analysis of (1): it follows from assumptions (i)–(iii) that there is a value $M>0$ such that

$$0 < \int_R \omega_{EE}(x')dx' + \alpha \int_R \omega_{IE}(x')dx' + \gamma(x) + \Psi(x,t) \leqslant M \quad \text{for all } x \text{ and } t \geqslant 0, \tag{A7}$$

$$0 \leqslant \beta = \frac{\gamma(x)}{\theta_1 - \theta_3} - 1 \leqslant K = L - 1 \quad \text{for all } x. \tag{A8}$$

2. The analysis

Here, we determine the effects of the activation factors $\eta(x)$ and $\gamma(x)$, and the stimulus Ψ on the dynamics of (1). The analysis consists of the following three steps:

(I) From (1) and (A2), and assumptions (i)–(iii) it follows that

$$E_t(x,0) = \gamma(x) > 0, \quad R_t(x,0) = 0,$$

$$I_t(x,0) = \eta(x) > 0 \quad \text{for all } x. \tag{A9}$$

Thus, E and I begin to increase as t increases from $t=0$. Below we show that if $\eta(x)$ is uniformly large then I quickly increases and exceed its threshold level θ_2. For this we define the reference point

$$T_0 = \ln\left(1 + \frac{\theta_1}{K\theta_1 + 2M}\right), \tag{A10}$$

where $M>0$ and $K>0$ satisfy Eqs. (A7) and (A8). Throughout, our analysis will make use of the observation that T_0 is independent of $\eta(x)$.

(II) We need the following estimates:

$$|E| \leqslant \left(\frac{K\theta_1}{2} + M\right)(e^t - 1) \leqslant \frac{\theta_1}{2} \quad \text{and } |R| \leqslant \varepsilon K \frac{\theta_1}{2}(1 - e^{-\varepsilon t}) \quad \text{for all } x \text{ and } 0 \leqslant t \leqslant T_0. \tag{A11}$$

To prove Eq. (A11) we begin with the following observation: for $t \geqslant 0$, as long as $|E| \leqslant \frac{\theta_1}{2}$ then the equation for R in Eq. (1) reduces to

$$-\varepsilon K \frac{\theta_1}{2} \leqslant R_t + \varepsilon R \leqslant \varepsilon K \frac{\theta_1}{2} \quad \text{for all } x \text{ and } t \geqslant 0. \tag{A12}$$

Multiply Eq. (A12) by $e^{\varepsilon t}$, integrate from 0 to t, and obtain

$$-\frac{K\theta_1}{2}(1 - e^{-\varepsilon t}) \leqslant R(x,t) \leqslant K\frac{\theta_1}{2}(1 - e^{-\varepsilon t}) \quad \text{for all } x \text{ and } t \geqslant 0. \tag{A13}$$

Next, it follows from the first equation in Eq. (1), and the global bound (A7), that

$$-M + R \leqslant E_t + E \leqslant M + R \quad \text{for all } x \text{ and } t \geqslant 0. \tag{A14}$$

Substitution of Eqs. (A13) into (A14) gives

$$-\frac{K\theta_1}{2}(1 - e^{-\varepsilon t}) - M \leqslant E_t + E \leqslant M + \frac{K\theta_1}{2}(1 - e^{-\varepsilon t}), \tag{A15}$$

which holds for $t \geqslant 0$ as long as $|E| \leqslant \frac{\theta_1}{2}$. Finally, we multiply Eq. (A15) by e^t, integrate from 0 to t, rearrange terms, and conclude that

$$|E(x,t)| \leqslant \left(K\frac{\theta_1}{2} + M\right)(e^t - 1) \leqslant \frac{\theta_1}{2} \quad \text{for all } x \text{ and } t \in [0, T_0]. \tag{A16}$$

This completes the proof of Eq. (A11).

Remark. The estimates in Eqs. (A13) and (A16) hold uniformly with respect to x and $t \in [0, T_0]$. These bounds also guarantee that $|E(x,t)|$ and $|R(x,t)|$ remain uniformly small over short intervals of time.

(III) We now determine the behavior of $I(x,y,t)$ over the interval $0 \leq t \leq T_0$. From Eqs. (1) and (A4) it follows that $I(x,y,t)$ satisfies $\tau I_t + I \geq (1+\delta)\theta_2$. Solving this differential inequality gives $I(x,t) \geq (1+\delta)\theta_2(1-e^{-t/\tau})$ for $t \geq 0$ since $I(x,0)=0$. At $t=\tau \ln((1+\delta)/\delta)$ we have

$$I\left[x, \tau \ln\left(\frac{(1+\delta)}{\delta}\right)\right] \geq \theta_2 \quad \text{for all } x.$$

Therefore, there is a minimal $T^* \in [0, \tau \ln\{(1+\delta)/\delta\}]$ such that

$$I(x,t) \geq \theta_2 \quad \text{for all } x \text{ and } x \geq T^*. \tag{A17}$$

Remark. Property (A17) represents the population of inhibitory neurons becoming tonically active at $t=T^*$, and remaining tonically active for all $t \geq T^*$ [18,22]. Below, we analyze the most important implications of Eq. (A17) for the system's dynamics.

First, note that inequality $0 < T^* < \tau \ln[(1+\delta)/\delta]$ causes

$$T^* \to 0 \text{ as } \delta \to \infty. \tag{A18}$$

In particular, we let δ be large enough so that $0 < T^* < T_0$, where T_0 is the reference point defined in Eq. (A10). Next, it follows from Eq. (A17) that the Heaviside function $f[I(x,t) - \theta_2]$ satisfies

$$f[I(x,t) - \theta_2] = 1 \quad \text{for all } x \text{ and } t \geq T^*. \tag{A19}$$

It is important to observe that property (A19) implies that

$$\int_R \omega_{IE}(x-x') f(I-\theta_2) dx' = \int_R \omega_{IE}(x') dx' \quad \text{for all } x \text{ and } t \geq T^*. \tag{A20}$$

The baseline state system. Because of Eq. (A20), observe that when $T^* \leq t < T_0$, the (E,R) component of the solution of Eq. (1) satisfies

$$\frac{\partial E}{\partial t} = -E - R + \int_R \omega_{EE}(x-x') f(E-\theta_1) dx' - \alpha \int_R \omega_{IE}(x') dx' dy' + \gamma(x) + \Psi,$$

$$\frac{\partial R}{\partial t} = \varepsilon(\beta E - R). \tag{A21}$$

Below, we explain the effects of the different components of Ψ on the dynamics of Eq. (A21). Our goal is to describe the time sequence of events that transforms Eq. (A21) to the time-varying baseline state. In particular, we will show how our choice of Ψ causes the form of system (A21) to undergo a sequence of switches at the times T_1 and T_2 which satisfy [see (2) and Table I]

$$T^* < T_1 < T_2 < T_0. \tag{A22}$$

First, recall that $\Psi(x,y,t)=0$ on the interval $T^* \leq t < T_1$ (Table I, part II), hence Eq. (A21) becomes

$$\frac{\partial E}{\partial t} = -E - R + \int_R \omega_{EE}(x-x') f(E-\theta_1) dx' - \alpha \int_R \omega_{IE}(x') dx' + \gamma(x),$$

$$\frac{\partial R}{\partial t} = \varepsilon(\beta E - R). \tag{A23}$$

The dynamic behavior of E and R is governed by Eq. (A23) when $T^* \leq t < T_1$.

Switch 1. At $t=T_1$ the stimulus changes from $\Psi=0$ to $\Psi = \alpha \int w_{IE}$, and this causes (A21) to switch its form from Eq. (A23) to

$$\frac{\partial E}{\partial t} = -E - R + \int_R \omega_{EE}(x-x') f(E-\theta_1) dx' + \gamma(x),$$

$$\frac{\partial R}{\partial t} = \varepsilon(\beta E - R). \tag{A24}$$

We refer to Eq. (A24) as an excitable system (Table I, part III) since ω_{EE} only describes connections between populations of excitable neurons, and the activity I of the inhibitory neurons plays no role in its dynamics when $t \geq T_1$ [13]. The dynamic behavior of E and R is governed by Eq. (A24) when $T_1 \leq t < T_2$. Note that the system is inactive since $E < \theta_1$ on $T_1 \leq t < T_2$.

Switch 2. At $t=T_2$, we add a strong, instantaneous stimulus ζ to the previously applied stimulus $\Psi = \alpha \int w_{IE}$. We let ζ satisfy

$$\zeta(x,t) = \begin{cases} Ae^{-(x^2)}, & t = T_2, \\ 0, & t > T_2. \end{cases} \tag{A25}$$

This causes Eq. (A24) to switch its form to

$$\frac{\partial E}{\partial t} = -E - R + \int_R \omega_{EE}(x-x') f(E-\theta_1) dx' + \gamma(x) + \zeta(x,t),$$

$$\frac{\partial R}{\partial t} = \varepsilon(\beta E - R). \tag{A26}$$

When $t \geq T_2$ the dynamic behavior of E and R is governed by Eq. (A26). To analyze the dynamics of Eq. (A26), it is convenient to rescale the variables and parameters by setting

$$u = E - \frac{\gamma(x,y)}{1+\beta}, \quad v = R - \frac{\beta\gamma(x,y)}{1+\beta},$$

$$\omega = \omega_{EE}, \quad \theta = \theta_1 - \frac{\gamma(x,y)}{1+\beta}. \tag{A27}$$

This transforms (A26) into the canonical, excitable form of Eq. (4).

Recall from Eq. (A6) that $\beta=\frac{\gamma(x)}{\theta_1-\theta_3}-1$. This, and Eq. (A27) imply that $\theta=\theta_3$ in Eq. (4). The dynamic behavior of system (4) depends on the stimulus ζ and the functional form of β. Detailed analysis of the behavior of Eq. (4) in different ranges of constant values of β is described in Sec. II A and II B the effects of spatially variable β are shown in Sec. II C. In these sections we show that there is a critical value of β^* such that, when $\beta \geqslant \beta^*$, large-scale synchronous oscillations occur when $\zeta(x,T_2)$ is of sufficient magnitude. Other types of functional activity that arise when $\beta<\beta^*$ are also described in the main body of the manuscript. Since we apply stimulus ζ at time $t=T_2$, we need to estimate the values of u and v at $t=T_2$. It follows from Eqs. (A6) and (A27) that

$$u(x,T_2) = E(x,T_2) - (\theta_1 - \theta_3),$$

$$v(x,T_2) = R(x,T_2) - [\gamma - (\theta_1 - \theta_3)]. \tag{A28}$$

From Eqs. (A13) and (A16) we conclude that

$$|E(x,T_2)| \ll K\frac{\theta_1}{2} \quad \text{and} \quad |R(x,T_2)| \ll K\frac{\theta_1}{2}. \tag{A29}$$

From Eqs. (A28) and (A29) we obtain the estimate

$$-\frac{3\theta_1}{2} + \theta_3 \leqslant u(x,T_2) \leqslant -\frac{\theta_1}{2} + \theta_3. \tag{A30}$$

Since we assume [see (ii)] that $\theta_3 \approx \theta_1$ and $\theta=\theta_3$, we can approximate Eq. (A30) with

$$|u(x,T_2)| \ll \frac{\theta}{2} \quad \text{for all } x. \tag{A31}$$

Similar reasoning gives the estimate

$$|v(x,T_2)| \ll K\frac{\theta}{2} \quad \text{for all } x. \tag{A32}$$

The estimates given in Eqs. (A31) and (A32) imply that $u(x,T_2)$ and $v(x,T_2)$ are approximately zero when $T_2-T^*>0$ is small. Hence, for computational simplicity we assume that

$$u(x,T_2) = v(x,T_2) = 0 \quad \text{for all } x. \tag{A33}$$

At T_2 we apply the stimulus $\zeta(x,T_2)$ to the system (4) with initial values given in (A33). If the stimulus $\zeta(x,T_2)$ is strong enough and β is in an appropriate range, synchronous self-sustained oscillations are initiated at the point of stimulus and spread outward. The detailed description of this process is given in the main body of the manuscript.

[1] G. Buzsaki, *Rhythms of the Brain* (Oxford University Press, Oxford, 2006).
[2] G. Buzsaki and A. Draguhn, Science **304**, 1926 (2004).
[3] *Epilepsy as a Dynamic Disease*, edited by J. Milton and P. Jung, Biological and Medical Physics series (Springer, Berlin, 2003).
[4] N. K. Logothetis and J. Pfeuffer, Magn. Reson. Imaging **22**, 1517 (2004).
[5] B. D. Burns, J. Physiol. (London) **112**, 156 (1951).
[6] Y. Adini, D. Sagi, and M. Tsodyks, Proc. Natl. Acad. Sci. U.S.A. **94**, 10426 (1997).
[7] P. A. Robinson, C. J. Rennie, D. L. Rowe, S. C. O'Connor, J. J. Wright, E. Gordon, and R. W. Whitehouse, Neuropsychopharmacology **28**, Suppl 1:S74 (2003).
[8] V. L. Towle, F. Ahmad, M. Kohrman, K. Hecox, and S. Chkhenkeli, in *Epilepsy as Å Dynamic Disease* [3], pp. 69–81, adapted with permission.
[9] J. A. Hobson and R. W. McCarley, Am. J. Psychiatry **134**, 1335 (1977).
[10] Y. Tsau, L. Guan, and J. Y. Wu, J. Neurophysiol. **80**, 978 (1998).
[11] H. R. Wilson and J. D. Cowan, Biophys. J. **12**, 1 (1972).
[12] H. R. Wilson and J. D. Cowan, Kybernetik **13**, 55 (1973).
[13] D. Pinto and G. B. Ermentrout, SIAM J. Appl. Math. **62**, 206 (2001).
[14] D. Pinto, R. Jackson, and C. E. Wayne, SIAM J. Appl. Dyn. Syst. **4**, 954 (2005).
[15] W. C. Troy and V. Shusterman, SIAM J. Appl. Dyn. Syst. **6**, 263 (2007).
[16] D. A. Gusnard and M. E. Raichle, Nat. Rev. Neurosci. **2**, 685 (2001).
[17] M. E. Raichle and M. A. Mintun, Annu. Rev. Neurosci. **29**, 449 (2006).
[18] R. S. Sloviter, Epilepsy Curr. **3**, 3 (2003).
[19] *Electroencephalography: Basic Principles, Clinical Applications, and Related Fields*, edited by E. Niedermeyer and F. Lopes da Silva (Lippincott Williams & Wilkins, Baltimore, MD, 2005).
[20] *Neocortical Dynamics and Human EEG Rhythms*, edited by P. L. Nunez (Oxford University Press, Oxford, 1995).
[21] I. Bojak and D. T. J. Liley, Phys. Rev. E **71**, 041902 (2005).
[22] K. A. Richardson, S. J. Schiff, and B. J. Gluckman, Phys. Rev. Lett. **94**, 028103 (2005).
[23] D. Pinto and W. C. Troy (unpublished).
[24] F. H. Lopes da Silva, J. P. Pijn, and W. J. Wadman, Prog. Brain Res. **102**, 359 (1994).
[25] X. Huang, W. C. Troy, Q. Yang, H. Ma, C. R. Laing, S. J. Schiff, and J. Y. Wu, J. Neurosci. **24**, 9897 (2004).
[26] G. B. Ermentrout, Rep. Prog. Phys. **61**, 353 (1998).
[27] K. Kang, M. Shelley, and H. Sompolinsky, Proc. Natl. Acad. Sci. U.S.A. **100**, 2848 (2003).
[28] S. Folias and P. Bressloff, Phys. Rev. Lett. **95**, 208107 (2005).
[29] S. Folias and P. Bressloff, SIAM J. Appl. Dyn. Syst. **3**, 378 (2004).
[30] P. Blomquist, J. Wyller, and G. T. Einevoll, Physica D **206**, 180 (2005).
[31] *Textbook Of Medical Physiology*, 10th ed., edited by A. C. Guyton and J. E. Hall (W. B. Saunders Company, Philadelphia, 2000).
[32] J. R. Gibson, M. Beierlein, and B. W. Connors, Nature (Lon-

don) **402**, 75 (1999).
[33] A. Destexhe and D. Contreras, Science **314**, 85 (2006).
[34] J. J. Pang, F. Gao, and S. M. Wu, J. Neurosci. **23**, 6063 (2003).
[35] H. R. Wilson, R. Blake, and S.-H. Lee, Nature (London) **412**, 907 (2001).
[36] C. S. Peskin, Mathematical aspects of heart physicology, New York: *Courant Inst. Math. Sci. Pub.* 268 (1973).
[37] R. E. Mirollo and S. H. Strogatz, SIAM J. Appl. Math. **50**, 1645 (1990).
[38] M. Vreugdenhil, E. Bracci, and J. G. Jefferys, J. Physiol. (London) **562**, 149 (2005).
[39] M. N. Titulaer, W. Kamphuis, C. W. Pool, J. J. van Heerikhuize, and F. H. Lopes da Silva, Neuroscience **59**, 817 (1994).
[40] M. G. Knyazeva, E. Fornari, R. Meuli, and P. Maeder, J. Neurophysiol. **96**, 259 (2006).
[41] I. Ferezou, S. Bolea, and C. C. Petersen, Neuron **50**, 617 (2006).
[42] I. Bojak and D. T. J. Liley, Neurocomputing **70**, 2085 (2007).
[43] W. Gerstner and W. M. Kistler, *Spiking Neuron Models: Single Neurons, Populations, Plasticity* (Cambridge University Press, Cambridge, 2002).
[44] S. Coombes, Biol. Cybern. **93**, 91 (2005).
[45] D. Mcmillen and N. Kopell, J. Comput. Neurosci. **15**, 143 (2003).
[46] J. Garcia-Ojalvo, M. B. Elowitz, and S. H. Strogatz, Proc. Natl. Acad. Sci. U.S.A. **101**, 10955 (2004).
[47] P. Suffczynski, S. Kalitzin, G. Pfurtscheller, and F. H. Lopes da Silva, Int. J. Psychophysiol **43**, 25 (2001).
[48] M. T. Wilson, J. W. Sleigh, D. A. Steyn-Ross, and M. L. Steyn-Ross, Anesthesiology **104**, 588 (2006).
[49] V. Shusterman, B. Aysin, V. Gottipaty, R. Weiss, S. Brode, D. Schwartzman, and K. P. Anderson, J. Am. Coll. Cardiol. **32**, 1891 (1998).
[50] V. Shusterman, K. P. Anderson, and O. Barnea, Am. J. Physiol. Regulatory Integrative Comp. Physiol. **273**, R1173 (1997).
[51] W. A. Janczewski and J. L. Feldman, J. Physiol. (London) **570**, 407 (2006).
[52] See Supplementary movies S1, S2, S3, S4, S5, at: http://www.math.pitt.edu/~troy/sync/